POLITECNICO DI TORINO
Repository ISTITUZIONALE

Additive and formative manufacturing of candidate abiotic materials for cardiovascular and neurovascular tissues

Original
Additive and formative manufacturing of candidate abiotic materials for cardiovascular and neurovascular tissues / Civilla, L., Riviello, M., Montiel-Saletovic, I., Unger, E., Königshofer, M., Gursoy, A., Mäder, L., Jaksa, L., Lorenz, A., Kornfellner, E., Gallo, D., Moscato, F.. - In: MATERIALS TODAY COMMUNICATIONS. - ISSN 2352-4928. - 57:(2026). [10.1016/j.mtcomm.2026.116579]

Availability:
This version is available at: 11583/3017997 since: 2026-11-18T15:21:25Z

Publisher:
Elsevier

Published
DOI:10.1016/j.mtcomm.2026.116579

Terms of use:

This article is made available under terms and conditions as specified in the corresponding bibliographic description in the repository

Publisher copyright

(Article begins on next page)

22 November 2026

Materials Today Communications 57 (2026) 116579

Contents lists available at ScienceDirect

Materials Today Communications

journal homepage: www.elsevier.com/locate/mtcomm

Additive and formative manufacturing of candidate abiotic materials for cardiovascular and neurovascular tissues

Lorenzo Civilla [a,b,1], Maria Riviello [b,c], Itzany Montiel-Saletović [b,d], Ewald Unger [b,2], Markus Königshofer [b,3], Akin Gursoy [e,4,5], Luis Mäder [e,5], Laszlo Jaksa [d,f,6], Andrea Lorenz [f,7], Erik Kornfellner [b,g,8], Diego Gallo [c,9], Francesco Moscato [a,b,h,*,10]

[a] Ludwig Boltzmann Institute for Cardiovascular Research, Vienna, Austria
[b] Center for Medical Physics and Biomedical Engineering, Medizinische Universität Wien, Vienna, Austria
[c] Department of Mechanical and Aerospace Engineering, Politecnico di Torino, Torino, Italy
[d] Institute of Lightweight Design and Structural Biomechanics, Technische Universität Wien, Vienna, Austria
[e] Spectroplast AG, Zurich, Switzerland
[f] Anatomical Models, ACMIT Gmbh (Austrian Center for Medical Innovation and Technology), Wiener Neustadt, Austria
[g] University of Applied Sciences Technikum Vienna, Vienna, Austria
[h] Austrian Cluster for Tissue Regeneration, Vienna, Austria

ARTICLE INFO

Keywords:
Material Characterization
Hardness Tests
Needle Puncturing Tests
Uniaxial Tensile Tests
Medical Simulation

ABSTRACT

Background: The development of cardiovascular and cerebrovascular tissue replicas is crucial for medical simulation training and device testing. This study investigates manufacturing technologies and materials, mainly silicone based, to identify suitable candidates for such applications.
Methods: Several traditional and additive manufacturing materials commonly used for vessel phantoms were included. Mechanical characterization tests including shore hardness, uniaxial tensile and needle puncturing tests have been performed according to international standards. The collected data were fitted with isotropic constitutive models to complete the mechanical characterization.
Results: The statistical analysis revealed differences in the mechanical properties among the tested materials. Additionally, correlations between standard hardness and stacked dumbbells hardness results were observed. The investigated materials presented ranges of elastic moduli, stretch at rupture and hyperelasticity. Second-order Mooney Rivlin, second-order Ogden and Yeoh models provided good fit for most materials. Correlations among the measured parameters were identified. Comparison with biological values enabled development of a design map for material selection.
Conclusions: The study identifies materials that approximate properties of human blood vessels, making them promising candidates for creating high-fidelity cardiovascular and cerebrovascular phantoms. These findings have implications for development of more effective training models in medical education and can enhance the fidelity of surgical simulations.

* Correspondence to: Center for Medical Physics and Biomedical Engineering, Medical University of Vienna, Waehringer Guertel, Vienna 18-20 1090, Austria.
E-mail address: francesco.moscato@meduniwien.ac.at (F. Moscato).
[1] 0009-0004-5156-3716
[2] 0000-0003-0275-9988
[3] 0000-0003-4671-6701
[4] 0000-0001-5355-0776
[5] Spectroplast AG, Zurich, Switzerland changed legal form in Spectroplast GmbH, Munich, Germany. Akin Gursoy is currently not affiliated to Spectroplast AG nor GmbH. Luis Mäder currently affiliated at Heidenhain AG, Schwerzenbach, Switzerland.
[6] 0000-0002-3043-1536
[7] 0000-0002-9208-4701
[8] 0000-0001-5656-7063
[9] 0000-0002-7409-7111
[10] 0000-0003-0279-6615

https://doi.org/10.1016/j.mtcomm.2026.116579
Received 27 July 2026; Received in revised form 10 October 2026; Accepted 1 November 2026
Available online 6 November 2026
2352-4928/© 2026 The Authors. Published by Elsevier Ltd. This is an open access article under the CC BY license (http://creativecommons.org/licenses/by/4.0/).

1. Introduction

The advancement of medical simulations is essential for reducing the reliance on human testing in device development, training, and preoperative planning throughout the entire healthcare delivery value chain. [1,2] High-fidelity simulations facilitate the practice of complex procedures within a controlled and safe environment, thereby minimizing patient risks. [3] A pivotal component of these simulations is the use of realistic phantoms that accurately mimic human tissues and organs.

Vascular phantoms are critically important due to their broad range of applications, including ultrasound phantoms, skill refinement and retaining training, device testing, preoperative planning, prosthetics and graft development, drug delivery, microfluidics, mock loops, testing of robot-assisted surgeries, and various endovascular procedures. [4–11] Vascular phantoms are typically categorized as non-walled, walled, or full, depending if they constitute "channels" in a bulk matter, walls with inner lumen, or full lumen without a defined wall. [4,12] It is important to note that only the non-walled and walled phantoms are perfusable, usually with a blood-mimicking fluid. Vascular phantoms must replicate particular properties dependent on the specific application, such as visibility in ultrasound, magnetic resonance imaging, and computed tomography scans, biocompatibility, mechanical realism, haptic realism, and transparency. Among these properties, mechanical realism is the most fundamental. [13]

Vascular phantoms that mechanically mimic real anatomies have been extensively developed using various Vessel Mimicking Materials (VMM). Significant advancements in material science unlocked the production of mechanically realistic VMM structures with patient-specific designs, but with a lower limit in wall thickness of about 500 μm. [4,14–16] VMM structures with lower wall-thickness and patient-specific designs can be produced, albeit with a compromise in mechanical fidelity. [4,8,17–20] The simultaneous achievement of thin-walled, patient-specific geometry and mechanically accurate VMMs remains an unresolved challenge in materials manufacturing.

Recent advancements in additive manufacturing technologies have introduced new processes that hold promise for addressing these challenges. [21] However, a fundamental knowledge gap exists between the industry and the biomedical research field: on one hand, material properties are usually presented in terms of synthetic parameters, such as shore hardness, tensile strength, Young's modulus and elongation at break, which provide standardized reference points for material selection and application; on the other hand, biological tissues are described in terms of stress-strain curves, viscoelastic models and constitutive equations, to comprehensively describe the material's behaviour under various loading conditions. This discrepancy limits the direct translation of commercially available material specifications into meaningful criteria for biomedical phantom design. Moreover, recently introduced materials have not yet undergone comprehensive mechanical characterization. [22,23] These materials are particularly attractive due to their additive manufacturing processes offering great design freedom, enabling the fabrication of highly accurate, patient-specific replicas. Characterizing these materials is essential for establishing the knowledge required to first identify the most appropriate manufacturing technology, and then the most suitable material for every biomedical application. Although several studies report the mechanical properties of some of these materials, differences in specimen geometries, testing protocols, loading conditions, and analysis methods, making cross-study comparison difficult. [19,24,25] A comprehensive study evaluating multiple manufacturing technologies and materials within a common experimental framework is still lacking. Consequently, the criteria that should ultimately guide material selection for vascular phantoms remain insufficiently defined.

The aim of this study was to investigate and characterize the most commonly used and newly emerged materials for the production of vascular tissues. This study aimed at establishing selection criteria for professionals in both the industry and medical fields involved in creating walled VMM phantoms.

2. Materials and methods

2.1. Materials selection and samples preparation

Inorganic VMMs were included and grouped according to their manufacturing methods (Table 1, Supplementary): [5,20,21,26–29]

- Casting and Injection Molding (CIM), including Ecoflex 00–30, Dragon Skin 10 Medium, Fast and Very Fast (the latter with addition of Thi-Vex 5 wt%), Dragon Skin 30, Smooth-Sil 936 (Smooth-On, Inc., Macungie, PA, USA), Platsil Gel 00 (Polytek Development Corp.,

Table 1
Materials and methods included. Every manufacturing method considered is presented, from Casting and Injection Molding (CIM), Stereolithography (SLA), Material Jetting (MJ) and Direct Ink Writing (DIW). Every material is identified with its commercial name, and a description of its type follows, completed by a unique acronym indicating also the printing direction.

Manufacturing technology	Material	Type	Label
CIM	Dragon Skin 10 Medium	Two-component RTV platinum-cure silicone elastomer	DS10M
	Dragon Skin 10 Fast	Two-component RTV platinum-cure silicone elastomer	DS10F
	Dragon Skin 10 Very Fast	Two-component RTV platinum-cure silicone elastomer	DS10VF *$_{CIM}$
	Dragon Skin 30	Two-component RTV platinum-cure silicone elastomer	DS30
	Ecoflex 00–30	Two-component RTV platinum-cure silicone elastomer	EF30
	Kiwosil S35	Two-component RTV addition-crosslinking silicone	KS35
	Platsil Gel 00	Two-component RTV platinum-catalysed silicone gel	PG00
	SmoothSil 936	Two-component RTV platinum-cure silicone elastomer	SS936
	Sylgard 184	Two-component PDMS silicone elastomer	S184
SLA	Elastic 50 A	SLA-printable elastomeric photopolymer resin; silicone-like, not silicone	E50Axy E50Axz E50Azx
	Silicone 40 A	SLA-printable pure silicone resin	S40Axy S40Azx
	TrueSil 20 A	3D-printable pure/true silicone elastomer	TS20Axy TS20Azx
	TrueSil 35 A	3D-printable pure/true silicone elastomer	TS35Axy TS35Azx
	TrueSil 50 A	3D-printable pure/true silicone elastomer	TS50Axy TS50Azx
	TrueSil 60 A	3D-printable pure/true silicone elastomer	TS60Axy TS60Azx
MJ	Agilus 30	PolyJet rubber-like photopolymer resin; not silicone	A30xy A30xz A30yx
	TangoPlus	PolyJet rubber-like photopolymer resin; not silicone	TPxy TPxz TPyx
DIW	Dragon Skin 10 Very Fast	Two-component RTV platinum-cure silicone elastomer	DS10VF *$_{DIW}$
	AMSIL 20101	Single-component, crosslinking liquid silicone rubbers	AM01

* addition of 5% wt Thi-Vex

Easton, Pennsylvania, USA), Kiwosil S35 (Kurt Wolf & Co., Vienna, Austria), Sylgard 184 (Dow, Midland, MI, USA). [28–30]

- ➢ Stereolithography (SLA), including Elastic 50 A, Silicone 40 A (Formlabs Inc., Somerville, MA, USA) and TrueSil 20 A, 35 A, 50 A and 60 A (Spectroplast AG, Zurich, Switzerland);
- ➢ Material Jetting (MJ), including the materials TangoPlus FullCure 930 and Agilus 30 (Stratasys Ltd., Eden Prairie, MN, USA);
- ➢ Direct Ink Writing (DIW), including Dragon Skin 10 Very Fast with additive Thi-Vex 5 wt% (Smooth-On, Inc.) and Amsil 20101 (Elkem Silicones, Saint-Fons, France)

Three different VMM testing sample designs were modelled in Fusion 360 (Autodesk, California, USA): a rounded square design (50 mm side x 8 mm thickness) for hardness tests according to standard ISO 48–4:2018 (Fig. 1A, B); a cylindrical design (35 mm diameter x 20 mm thickness; Fig. 1C, D); a dogbone design according to ISO 37:2017, Type 1 (115 mm length x 25 mm width x 2 mm thickness; Fig. 1E, F). Molds were produced with 3D printers Form 3B (Formlabs Inc.) and Ultimaker 3 (Ultimaker, Utrecht, Netherlands), as well as laser cutting of polymethyl methacrylate, and then used to produce samples of CIM materials. Material samples of SLA, MJ and DIW were produced with direct 3D printing in different directions with Form 3B (Formlabs Inc.), Connex3 Objet500 (Stratasys Ltd.), and a vipro-HEAD 3/3 two-component printhead (ViscoTec GmbH, Töging am Inn, Germany; Fig. 1G, H). [22,31–33] Printing cost and accuracy limitations did not allow to 3D print the fully vertical dogbone samples of the materials Silicone 40 A and the TrueSil family, and limited the production of DIW samples only to the horizontal configuration.

2.2. Samples characterization

2.2.1. Hardness testing

Shore hardness tests were conducted using the durometers Model HBA 100–0 and Model HB0 100–0 (SAUTER GmbH, Basel-Stadt,

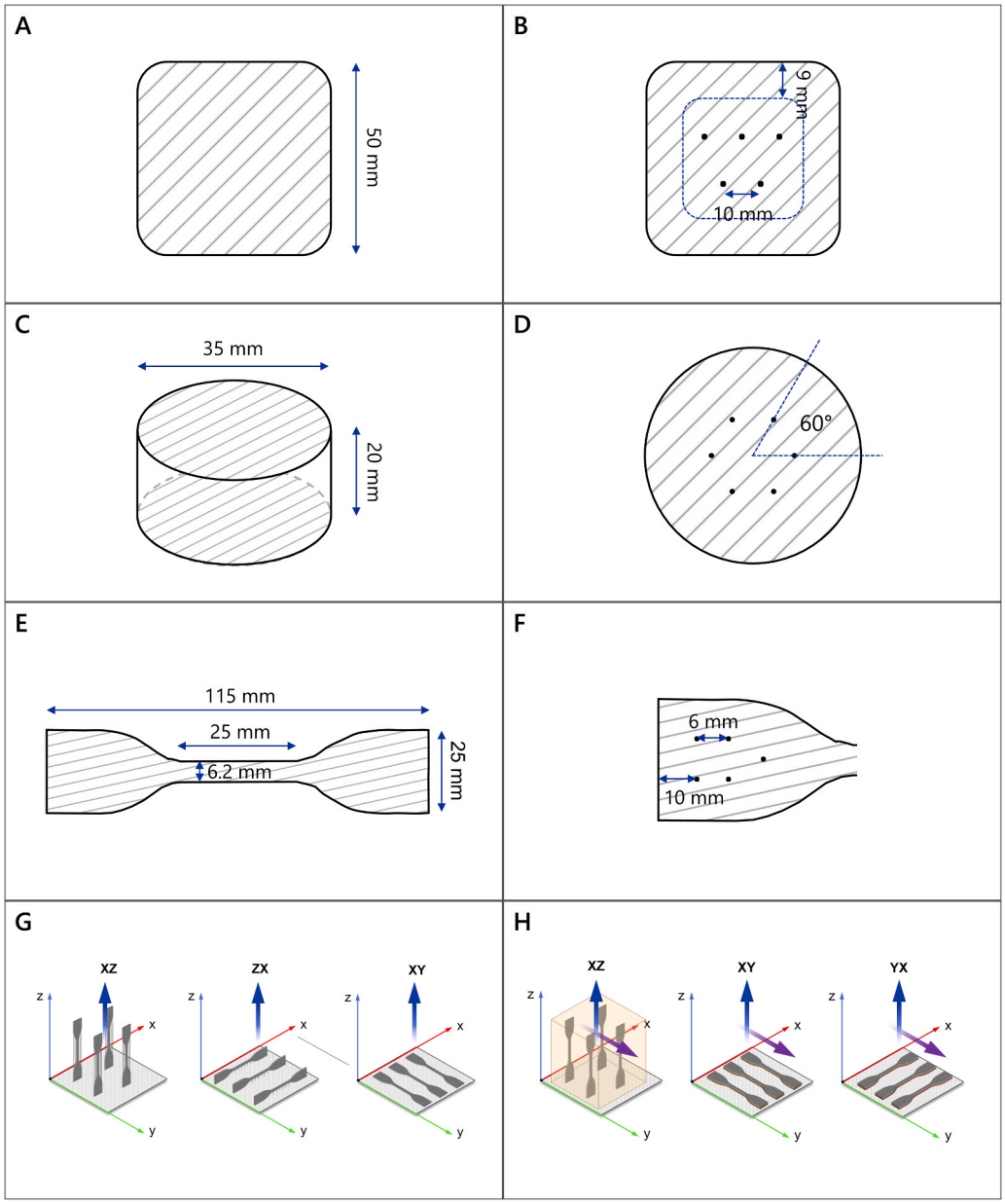


Fig. 1. CAD designs of the samples used for testing. (A) rounded square design; (B) indentation locations for hardness tests; (C) cylinder design and (D) locations for needle-puncturing tests; (E) dogbone design for uniaxial tensile tests and (F) indentation locations for hardness tests; (G) printing directions for SLA, DIW and (H) MJ with support structures. For the latter, the blue arrow identifies the layer deposition direction, while the purple arrow the jetting head movement direction.

Switzerland), measuring hardness respectively on the scales Shore A and Shore AO. The durometers were mounted on a linear stage equipped with a calibrated spring applying a constant pressure upon application of a weight of 1 kg, with the samples fixed on a rigid base beneath the durometer (Fig. 2A). Experiments were performed according to ISO 48–4:2018, and consisted of manually lowering the stage-mounted durometer on one (n = 1) rounded square and one (n = 1) stack of three dogbone samples per material, five times per sample and in locations distant at least 9 mm from the border of the samples and 6 mm from each other (Fig. 1B, F). Readings were done at 1 s and 15 s after sample indentation. The five measurements represented repeated, non-independent, within-specimen measurements, and were compared descriptively using their mean and variability.

2.2.2. Needle puncture testing

The needle-puncture test setup was adapted from Jafary *et al.* to use a 18-gauge sharp-tip (length: 40 mm) luer-locked on a 3D printed head (Clear v4.1, Formlabs; $E = 2369$ MPa) connected to a 1 kN load cell measuring forces active on the needle at 200 Hz (KM26z-1kN; ME-Meßsysteme GmbH, Hennigsdorf, Germany) and mounted on an actuator (Fig. 2B). [5] One (n = 1) cylindrical shaped sample per material was fixed on a rigid base beneath the needle tip, which was then lowered and raised at a speed of 1 mm/s to puncture each sample four times in six different locations, with a rotation of 60° between locations (Fig. 1D). The six locations represented repeted within-specimen measurements and were not considered independent replicates. Measured forces were differentiated between puncture force, obtained as the peak force of the first puncturing cycle, friction force (F_{fri}), derived as the minimum of the first puncturing cycle, and cutting force (F_{cut}), obtained as difference between puncturing force and friction force, representing the force needed to cut the channel of the needle. The results were then reported as mean and standard deviation, and used for descriptive comparison.

2.2.3. Uniaxial tensile testing

A universal tensile testing machine (Beta 10–2,5; ZwickRoell Testing Systems GmbH, Fürstenfeld, Austria) was used to test the dogbone shaped samples (n = 5) fixed on self-tightening cylindrical grips attached to a 1 kN load cell (range: 0 – 1 kN; nominal sensitivity: 2 mV/V; AEP transducers, Cognento, Italy), according to the ISO 37:2017 standard (Fig. 2C). Experiments started with a pre-loading of 1 N, followed by extension of the samples at a constant rate of 500 mm/min until sample rupture, while optically acquiring elongation via fixed markers on the samples (Fig. 2C). All tests were performed at room temperature, and corrected for pre-loading stresses applied on the sample.

2.3. Data analysis and modelling

Data were imported and analysed in custom Python scripts and Excel Office Professional Plus 2019 (Microsoft Corp., Redmond, US), and reported as mean and standard deviation and coefficient of variation (CV). Hardness was compared between manufacturer reference values and measured, and between rounded square and stacked dumbbells designs (*t*-test, $\alpha = 0.05$, significance $p < 0.05$). Data from needle puncturing experiments were corrected for linear trend, filtered with a moving average filter (window size = 10 samples) and analysed: the maximum force represented the total puncturing force as sum of cutting and friction forces, the first one being the one necessary to pierce a channel in the material, and the second being the force of the lateral surface of the channel on the needle. The maximum friction force was calculated at the lowest peak of each puncturing cycle, and then subtracted from the puncturing force to derive the cutting force. Data from uniaxial tensile experiments were filtered with a moving average filter (window size = 10 samples), corrected for pre-loading and initial length (L_0) and then used to calculate both engineering and true strain and stresses, according to Eqs. 1 and 2:

$$\varepsilon_{eng} = \frac{L - L_0}{L_0}; \quad \varepsilon_{true} = \ln\left(\frac{L}{L_0}\right) \tag{1}$$

$$\sigma_{eng} = \frac{F}{A_0}; \quad \sigma_{true} = \frac{F}{A} \tag{2}$$

with L, F and A being the current length, measured force and cross-section, respectively.

The strain energy density function W was calculated, and the total strain energy was computed at rupture and indicated as W_{max}. Anisotropy as a function of strain was assessed through the Index of Anisotropy (I_A), computed as absolute difference over the average, of two different printing directions. Similarity analysis was performed as Euclidean distance in z-scored feature space using E_0, E_f, ε_{max}, σ_{max}, and W_{max}. To characterize the hyperelasticity of each material, a stiffening ratio

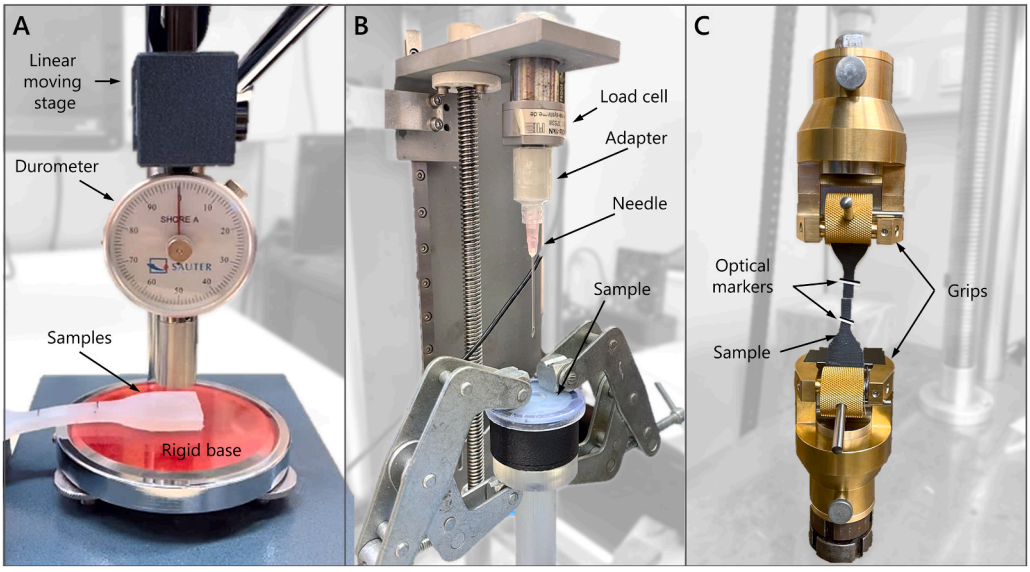


Fig. 2. Experimental setups. (A) Hardness test setup with stack of three dogbone samples; (B) needle puncture test setup with cylindrical sample; (C) uniaxial tensile test setup with sample after rupture.

comparing the initial and final moduli was computed. To provide a comparative benchmark, the mean curves of true stress and strain were used to fit isotropic, incompressible constitutive models, without shear contributions. The first isotropic model was a phenomenological polynomial model relating stress and strain:

$$\boldsymbol{\sigma} = \sum_{i=0}^{n} a_i \boldsymbol{E_H}^i \tag{3}$$

with $\boldsymbol{E_H}$ being the Hencky strain tensor collecting all the true strains $\varepsilon_{i,j}$. Without shear components, Eq. 3 was simplified as scalar and used for data fitting with $n = 1$ and $n = 2$. Additionally, the hypotheses $a_0 = 0$ and $\{a_0 = 0, a_1 = 0\}$ were assumed respectively in order to ensure interception of the origin and positive curvature. The second isotropic model implemented was a Neo-Hookean model (Eq. 4), appropriate for small strains: [34]

$$W = \frac{\mu}{2}(I_1 - 3) + \frac{K}{2}(J-1)^2 \tag{4}$$

with μ shear modulus, I_1 first invariant of the right Cauchy-Green deformation tensor $I_1 = \mathrm{tr}(\boldsymbol{C})$, and J determinant of $\boldsymbol{F}$ (in this case equal to 1). The third isotropic model was a Mooney-Rivlin model (Eq. 5) more suitable to capture large strains: [35,36]

$$W = \sum_{i,j=0}^{N} C_{i,j}(I_1 - 3)^i (I_2 - 3)^j + \sum_{i=1}^{N} K(J-1)^{2i} = C_{10}(I_1 - 3) + C_{01}(I_2 - 3) \tag{5}$$

with $C_{i,j}$ and K parameters of the model, and I_2 second invariant of the right Cauchy-Green deformation tensor $I_2 = 1/2\left((\mathrm{tr}(\boldsymbol{C}))^2 - \mathrm{tr}(\boldsymbol{C}^2)\right)$. The right hand term of Eq. 5 was obtained by assuming $N = 1$ (MR1) and $N = 2$ (MR2) and simplifying for incompressibility. The parameters were constrained to be non-negative. Further models included were the first and second order Ogden (OG1, OG2), third-order Yeoh (Y3) model, as well as Gent formulation, as described in eq.s 6, 7 and 8.

$$W = \sum_{p=1}^{N} \frac{\mu_p}{\alpha_p}(\lambda_1^{\alpha_p} + \lambda^{\alpha_p} + \lambda^{\alpha_p} - 3), \tag{6}$$

$$W = C_1(I_1 - 3) + C_2(I_1 - 3)^2 + C_3(I_1 - 3)^3, \tag{7}$$

$$W = -\frac{\mu J_m}{2} \ln\left(1 - \frac{I_1 - 3}{J_m}\right). \tag{8}$$

The root mean square error between data and model predictions was then calculated, and best fitting model per material selected. For correlation analysis, the material was considered the experimental unit. Each material contributed with a triplet of single values, one for each mechanical property: hardness and needle-puncture values were obtained by averaging repeated measurements performed on one specimen, while uniaxial tensile properties were averaged across the tested specimens and printing orientations. Pearson correlations were then calculated using these material-level values, with the effective sample size corresponding to the number of materials included in each analysis. Repeated within-specimen measurements and orientation-specific measurements were not treated as independent observations.

2.4. Comparison with biological reference data

The mechanical properties obtained from uniaxial testing of the investigated materials were compared with biological values obtained from literature (Supplementary) to evaluate the suitability of each material to replicate physiological or pathological cardiovascular and neurovascular structures. [37–44] Anatomical structures of interest included: physiological ascending aorta, coronary arteries, and cerebral arteries, as well as pathological ascending thoracic aortic aneurysms, atherosclerotic coronaries and intracranial aneurysms. While reference values were identified for needle puncturing forces and most of mechanical parameters, it was not possible to identify reference values for Shore hardness. Comparison was performed by comparing the engineering Young modulus against the biological reference intervals for low strain regime, and engineering strain, stress and modulus at failure with the corresponding biological reference intervals for the high-strain regime. Similarity was quantified using a normalized distance metric (d), defined as zero for values within the biological intervals and as the normalized distance from the nearest interval boundary for values outside the interval.

3. RESULTS

3.1. Shore hardness

The measured hardness on scales Shore A and AO on the rounded square samples ranged from 2.47 ± 0.33 to 55.24 ± 1.79 and from 10.20 ± 0.27 to 64.06 ± 2.79, respectively (Fig. 3). Measurements on the stack of three dogbone samples ranged between 2.98 ± 0.04 to 59.96 ± 0.05 in scale Shore A, and 11.8 ± 0.45 to 64.00 ± 0.95 in scale Shore AO. Given the high deformability of EF30, it was not possible to measure its hardness on the Shore A scale. When compared to the declared values from the manufacturers, the materials DS30, S184, S40A, TS20, TS35, TS50 and TS60 present a close match, with other CIM and DIW materials presenting a moderate deviation, and SLA and MJ materials presenting a higher deviation. Hardness values measured on rounded-square and stacked-dogbone specimens were generally comparable. At 1 s, relative differences ranged from 0 to 7.9% for Shore A and 0.1–14.9% for Shore AO. At 15 s, the ranges increased to 0.3–20.7% and 0–14.4%, respectively. The largest differences were observed for PG00, followed by DS10F and KS35, likely reflecting the greater measurement variability of softer materials (Supplementary).

3.2. Needle puncture

The results of the needle puncturing tests are periodic and present maximum and minimum values (Fig. 4A-D): for every material it is observed a high puncturing force on the needle on the first cycle, that then decreases cycle after cycle; the friction force appeared to stay constant over the duration of the experiments. The puncturing force ranged from 6.99 ± 0.05 N for PG00 to 54.13 ± 2.72 N for E50Axy (Fig. 4E). The friction force appears to be substantially higher than cutting force for every material, apart from EF30, for which the two are comparable. At a penetration depth of 0.5 mm in the sample, the measured forces were different and ranged from an average low of 0.12 N to a high value of 0.49 N, with a moderate variability (KS35: SD = 0.07 N; DS10VF: SD = 0.15 N), and only the material E50A resulted in a force in range with the biological reference value of 0.87 ± 0.23 N. [43] The measured force matched this biological range at an average penetration depth of 2.41 ± 0.55 mm, as shown in Supplementary.

3.3. Uniaxial tensile

Uniaxial tensile tests were performed successfully for every material, with at most one acquisition per material excluded due to sample slippage, allowing to calculate mechanical parameters and obtain all the true stress-strain curves (Fig. 5, Table 2). Experimental variability was generally very low with median CV in the range 0.023–0.099 for most (90%) of the materials, and few presenting higher variability (S40Axy: 0.222; TS20Axy: 0.145; TS35Axy: 0.311).

3.3.1. Single material properties

The mechanical responses ranged from highly compliant, low-energy materials (e.g., EF30: $\varepsilon_{max} = 0.915$, $\sigma_{max} = 2.018$ MPa, $W_{max} = 0.483$ MJ/m^3; TPxz: $\varepsilon_{max} = 0.537$, $\sigma_{max} = 0.628$ MPa, $W_{max} = 0.140$ MJ/m^3) to

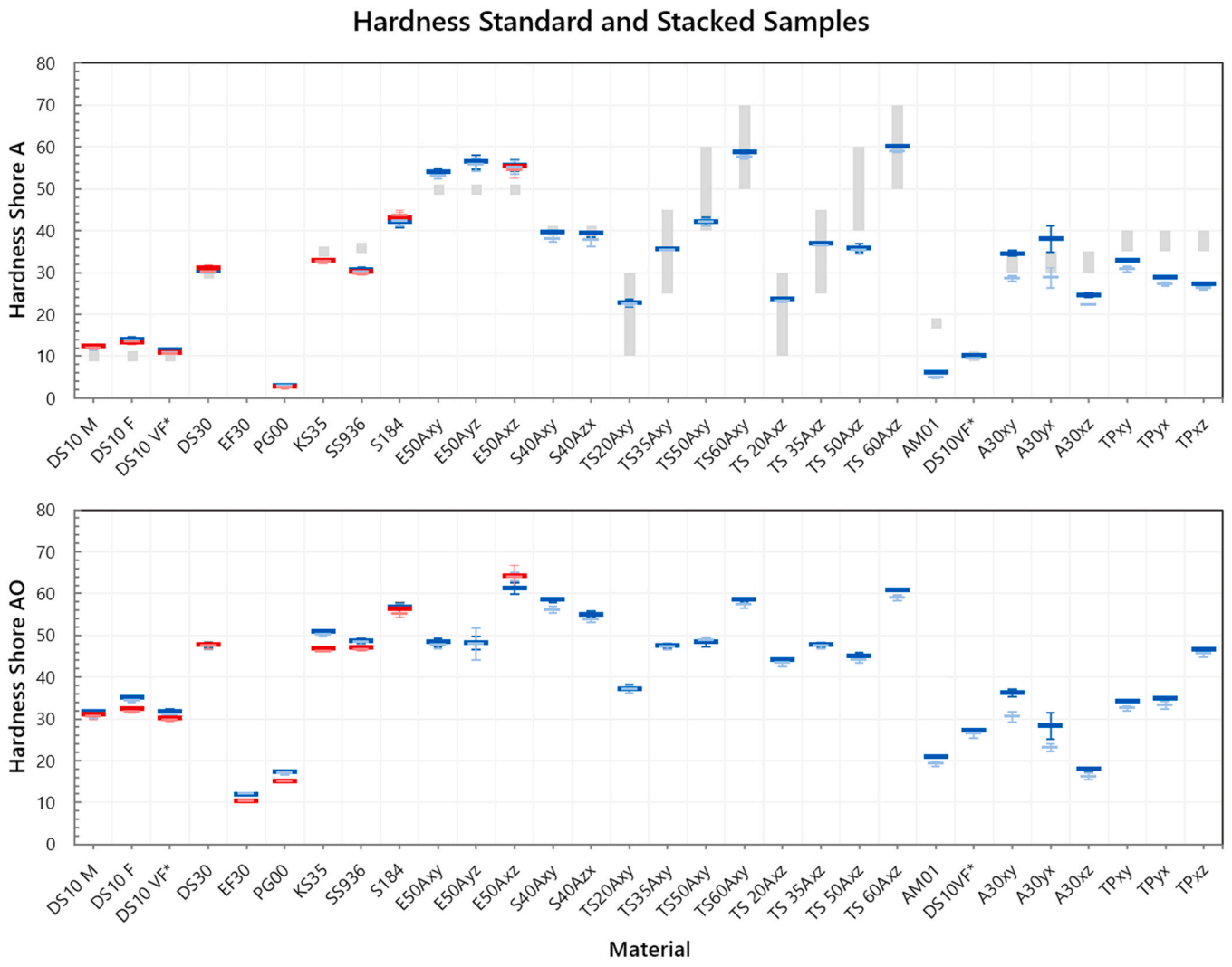


Fig. 3. Measured hardness. Scatter plot of the measured hardness for each material on scale Shore A (top panel) and Shore AO (bottom panel) on stacked dogbone samples (dark blue: 1 s; light blue: 15 s after indentation) and on rounded square samples (dark red: 1 s; light red: 15 s after indentation); grey: hardness ranges as indicated from the manufacturers.

very strong, highly energy-absorbing materials, particularly in SLA (e.g., SS936: $\varepsilon_{max} = 1.502$, $\sigma_{max} = 17.231$ MPa, $W_{max} = 6.315$ MJ/m^3; TS35Azx: $\varepsilon_{max} = 1.469$, $\sigma_{max} = 21.973$ MPa, $W_{max} = 6.363$ MJ/m^3; Fig. 6). Small-strain stiffness varied widely: the highest initial tangent modulus occurred for TS60Azx ($E_0 = 4.381$ MPa), whereas many CIM, MJ and DIW materials cluster around 0.1 – 0.7 MPa at small strain (e.g., DS10F 0.198 MPa; TPxz 0.657 MPa; AM01 0.033 MPa). Marked stiffening can be observed already at $\varepsilon = 0.18$ ($L = 1.2 * L_0$), with CIM materials stiffening of a factor of about 2, while SLA materials presenting a smaller stiffening. Not all materials reached $\varepsilon = 0.69$ ($L = 2 * L_0$), including S184, E50A (in all directions), S40Azx, TS60Azx, A30xz and TPxz. The most extensible material was TS35Axy ($\varepsilon_{max} = 1.557$) and the highest σ_{max} and W_{max} were observed for TS35Azx ($\sigma_{max} = 21.973$ MPa, $W_{max} = 6.363$ MJ/m^3), followed by other high-energy SLA materials including TS50Azx ($W_{max} = 5.760$ MJ/m^3) and TS35Axy ($W_{max} = 5.655$ MJ/m^3). Marked hyperelastic behaviour was observed for EF30 ($E_0 = 0.013$ MPa, $E_f = 4.818$ MPa), presenting a stiffening ratio of 371.237, and several SLA samples, especially TS20Azx (41.377) and TS35Axy (39.909), TS50Azx (31.798); in contrast, E50A resulted nearly linear over its measured range with minimal stiffening (0.960 – 1.562).

3.3.2. *Printing Orientation Anisotropy*

Orientation-dependent anisotropy was marked for SLA and moderate for MJ materials: TS35A showed the largest anisotropy, reaching an $I_{A,max}$ of 0.564 at $\varepsilon = 1.075$, with orientation-dependent differences becoming notable ($I_A \geq 0.15$) already from $\varepsilon = 0.015$ (Supplementary). TS20A also showed strong anisotropy ($I_{A,max} = 0.270$ at $\varepsilon = 1.360$), mainly in the high-strain regime, with differences becoming notable from $\varepsilon = 0.975$. S40A demonstrated moderate anisotropy ($I_{A,max} = 0.282$ at $\varepsilon = 0.535$) with notable divergence beginning around $\varepsilon = 0.345$, whereas TS60A showed higher anisotropy ($I_{A,max} = 0.306$ at $\varepsilon = 0.445$, notable from $\varepsilon = 0.010$). In contrast, TS50A exhibited initial notable anisotropy from a strain of 0.005 ($I_{A,max} = 0.202$), that decreased from a strain of 0.250 on, staying under the threshold of $I_A = 0.15$. E50A presented a monotonically decreasing I_A, from a starting value of 1.972 to under 0.15 at a strain of 0.365. For MJ materials, anisotropy was present but less pronounced than in the most anisotropic SLA cases: A30 reached $I_{A,max} = 0.333$ at $\varepsilon = 0.68$, with notable divergence only from $\varepsilon = 0.385$; TP showed slightly higher anisotropy, with $I_{A,max} = 0.323$ already at $\varepsilon = 0.015$ and higher than the I_A threshold for the whole strain range.

3.3.3. *Materials similarity*

The similarity analysis identified several clusters of mechanically interchangeable materials. Within MJ, A30 and TP presented a z-distance ranging from 0.186 to 0.684, making them highly comparable (E_0

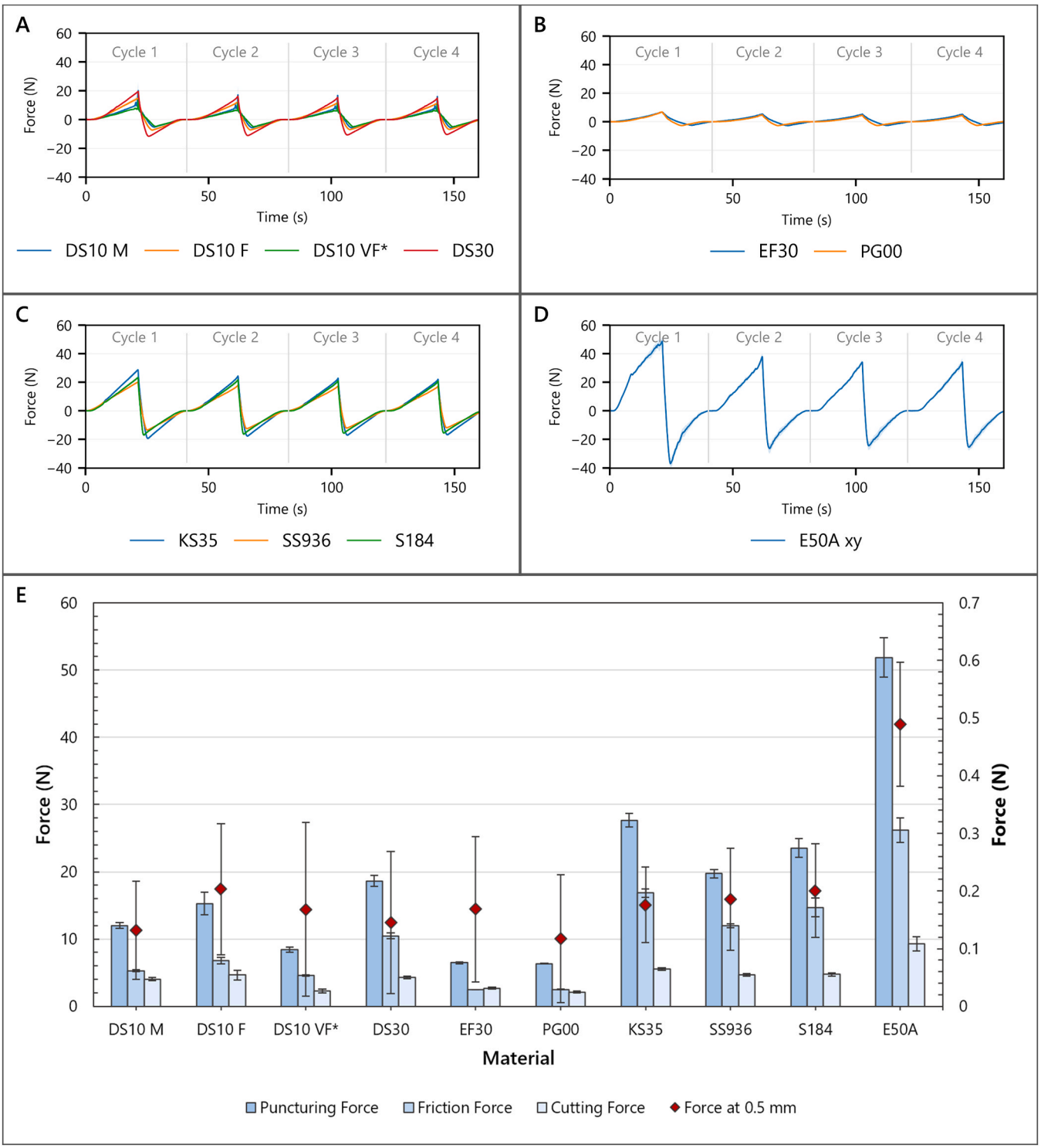


Fig. 4. Puncturing forces trends. Force trends of the tested materials (A-D), with positive values indicating compression of the force sensor upon needle puncturing in the sample, and negative values indicating elongation of the force sensor upon pulling of the needle from the sample. The zero intercept in the middle of every cycle identifies the moment of complete needle extraction. From the first cycle, the force components in magnitude and at a depth of 0.5 mm were calculated (E).

= 0.467 – 0.732 MPa; E_f = 1.455 – 6.401 MPa; ε_{max} = 0.537 – 0.750; σ_{max} = 0.628 – 2.203 MPa; W_{max} = 0.140 – 0.461 MJ/m^3). A notable cross-method equivalence appeared within the Dragonskin family: DS10M produced via CIM showed a z-distance of 0.118 with DS10VF produced via DIW (E_0 = 0.174 VS 0.179 MPa; E_f = 10.932 VS 11.493 MPa; ε_{max} = 1.465 VS 1.488; σ_{max} = 0.672 VS 0.641 MPa; W_{max} = 2.177 VS 2.291 MJ/m^3). At slightly higher distances, PG00 resulted similar to EF30 (0.296) and AM01 (0.347), and E50Azx resulted similar to S40Azx (0.516). Lower similarities were observed between TS20Axy and DS10VF produced via DIW (0.629), and DS10M via CIM (0.635), and between DS10F via CIM and PG00 (0.666) and AM01 (0.672).

3.3.4. *Constitutive modeling*

Model fitting to the mean true stress-strain curves resulted in high accuracy across materials, with R^2 ranging from 0.991 (S40Axy) to 0.999 (DS10VF), and RMSE between 0.001 MPa to 0.278 MPa, with

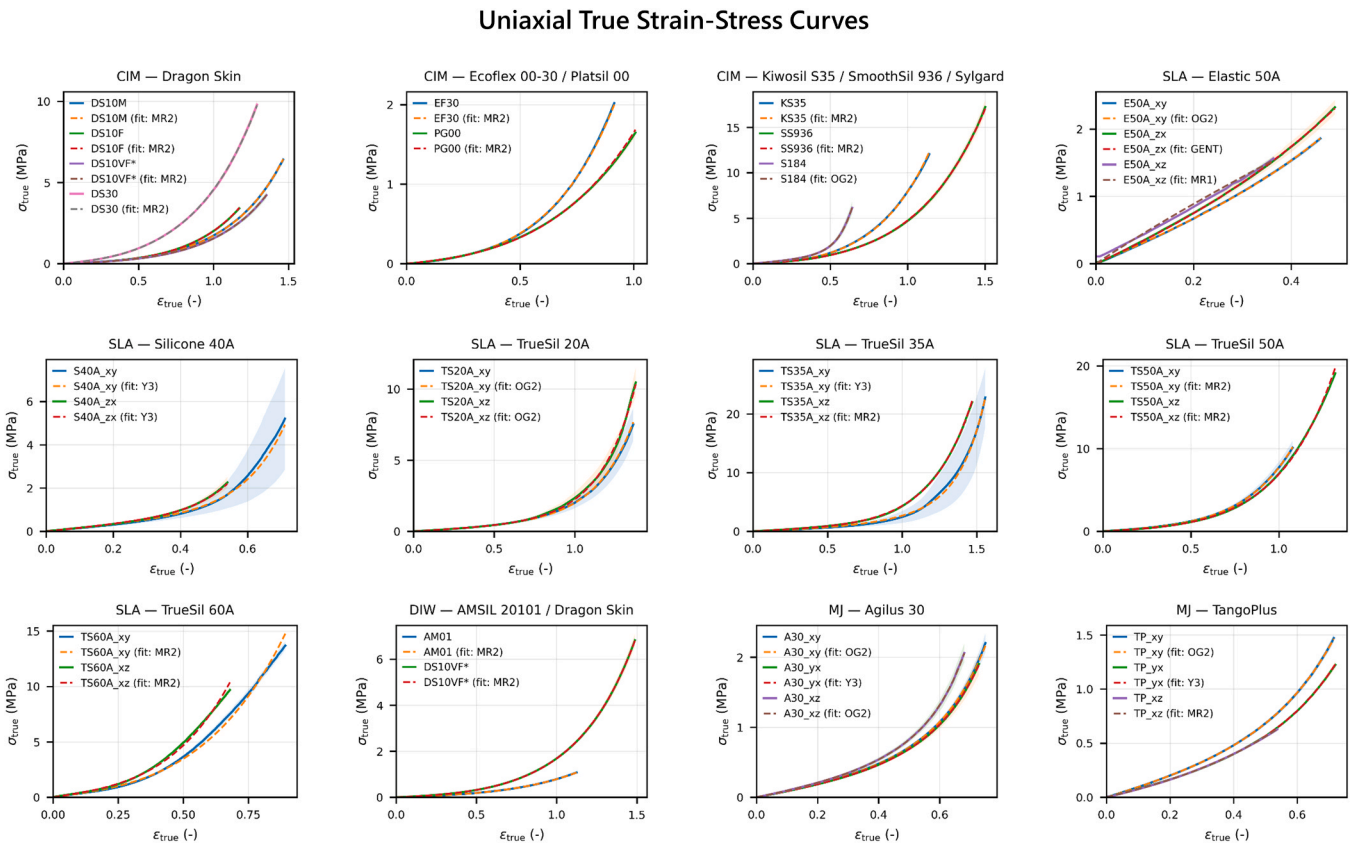


Fig. 5. Experimental true stress-strain curves. The stress-strain curves of materials are grouped by manufacturing technology and material family, displayed as mean true stress–strain curves with standard deviations (light blue shade). Best-fitting constitutive models are also overlaid as dotted lines.

Table 2
Mechanical properties of the investigated materials by manufacturing technology and both at low strains and failure. Not all materials reached an extension of 100%, for these materials the values $E_{100\%}$ and σ_{100} could not be computed.

Method	Material	E_0 (MPa)	$E_{20\%}$ (MPa)	$E_{100\%}$ (MPa)	E_{final} (MPa)	ε_{max} (-)	$\varepsilon_{eng,max}$ (-)	σ_{20} (MPa)	σ_{100} (MPa)	σ_{max} (MPa)	$\sigma_{eng,max}$ (MPa)	E_{final}/E_0 (-)	W (MJ/m^3)
CIM	DS10M	0.174	0.555	2.193	10.932	1.465	3.326	0.078	0.672	6.409	1.482	62.874	2.177
	DS10F	0.198	0.519	2.555	6.649	1.172	2.228	0.077	0.723	3.407	1.056	33.554	1.014
	DS10VF*	0.178	0.512	1.969	7.245	1.353	2.870	0.073	0.605	4.218	1.090	40.739	1.406
	DS30	0.682	1.377	5.933	16.683	1.290	2.634	0.204	1.860	9.792	2.694	24.451	3.372
	EF30	0.013	0.492	3.555	4.818	0.915	1.496	0.061	0.867	2.018	0.809	371.237	0.483
	KS35	0.639	1.437	10.276	24.394	1.140	2.126	0.202	2.727	12.049	3.854	38.190	3.463
	PG00	0.063	0.479	2.132	3.123	1.008	1.740	0.065	0.658	1.647	0.601	49.958	0.499
	SS936	0.676	1.291	6.209	26.677	1.502	3.491	0.191	1.898	17.231	3.837	39.444	6.315
	S184	1.178	2.095	-	27.070	0.642	0.900	0.315	-	6.138	3.231	22.971	0.822
SLA	E50Axy	1.795	3.595	-	4.182	0.460	0.584	0.604	-	1.859	1.174	2.330	0.381
	E50Axz	3.374	4.108	-	3.238	0.364	0.439	0.767	-	1.564	1.087	0.960	0.285
	E50Ayx	2.043	4.054	-	5.234	0.489	0.631	0.680	-	2.323	1.424	2.562	0.496
	S40Axy	1.586	1.637	23.988	19.586	0.711	1.036	0.279	4.662	5.204	2.556	12.350	0.848
	S40Azx	1.629	1.880	-	8.810	0.540	0.715	0.307	-	2.259	1.317	5.408	0.365
	TS20Axy	0.615	0.746	2.287	15.099	1.362	2.904	0.126	0.787	7.518	1.926	24.549	2.096
	TS20Azx	0.577	0.741	2.635	23.873	1.377	2.965	0.127	0.792	10.456	2.637	41.377	2.615
	TS35Axy	1.062	1.124	2.674	42.398	1.557	3.743	0.214	1.044	22.782	4.803	39.909	5.655
	TS35Azx	1.325	1.527	4.661	42.365	1.469	3.345	0.275	1.595	21.973	5.057	31.973	6.363
	TS50Axy	1.416	1.799	9.410	22.123	1.078	1.940	0.293	2.523	10.119	3.442	15.625	2.727
	TS50Azx	1.134	1.596	8.389	36.065	1.320	2.745	0.248	2.296	19.097	5.100	31.798	5.760
	TS60Axy	3.573	3.987	25.819	25.171	0.892	1.439	0.609	7.880	13.684	5.611	7.045	3.826
	TS60Azx	4.381	5.236	-	23.164	0.679	0.972	0.746	-	9.684	4.910	5.288	2.105
MJ	A30xy	0.636	1.075	8.105	6.401	0.750	1.116	0.171	1.642	2.203	1.041	10.072	0.461
	A30xz	0.732	1.179	-	6.667	0.681	0.975	0.186	-	2.061	1.044	9.110	0.396
	A30yx	0.615	1.034	7.880	5.549	0.729	1.072	0.166	1.590	1.904	0.919	9.027	0.403
	TPxy	0.657	1.112	2.560	3.599	0.715	1.044	0.181	1.351	1.471	0.719	5.482	0.362
	TPxz	0.467	0.942	-	1.455	0.537	0.712	0.146	-	0.628	0.367	3.118	0.140
	TPyx	0.549	0.910	4.013	3.039	0.720	1.054	0.149	1.113	1.223	0.595	5.533	0.305
DIW	DS10VF*	0.179	0.468	2.197	11.493	1.488	3.427	0.069	0.641	6.829	1.542	64.381	2.291
	AM01	0.033	0.315	1.002	1.827	1.124	2.077	0.045	0.342	1.077	0.350	54.829	0.369

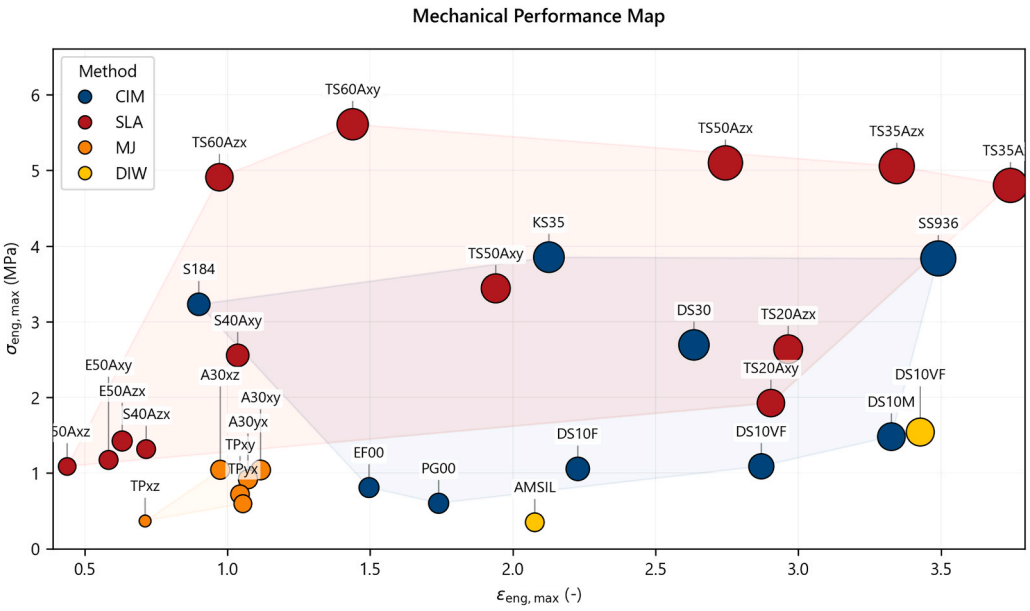


Fig. 6. Performance graph of the materials investigated in terms of maximum strain and stresses. Materials from CIM are shown in dark blue, SLA in dark red, MJ in orange, and DIW in yellow. Shaded areas identify manufacturing technologies and show the mechanical range: more limited for MJ and DIW; more expanded for CIM and SLA.

advanced Mooney-Rivlin, Ogden, Yeoh hyperelastic formulations required in 53.3%, 23.3% and 16.6% of the cases respectively, and two materials requiring a MR1 or Gent formulation (Supplementary). For most of CIM, SLA and DIW materials, the MR2 model represented the best-fitting model. The identified MR2 coefficients were homogeneously distributed over C10 (0.036 – 0.132 MPa), C01 (0.002 – 0.637 MPa), C11 (0.003 – 0.392 MPa), and C02 (0.009 – 0.487 MPa), with higher values observed in stiffer materials such as DS30 (C10 = 0.132 MPa) and TS60Azx (C01 = 0.637 MPa, C11 = 0.393 MPa), or in more hyperelastic materials like TS50Axy (C20 = 0.012 MPa), TS60xy (C02 = 0.487 MPa).

In contrast, several materials exhibiting pronounced strain stiffening were better captured by Ogden models. Sylgard 184 was well described by an OG2 model, with parameters $\mu_1 = 0.640$ MPa, $\alpha_1 = 1.511$ and $\mu_2 = 6.597 \times 10^{-3}$ MPa, $\alpha_2 = 10.876$, reflecting a dominant moderate exponent with a secondary high-exponent contribution. Also TS20A could be well described by the same model, with more balanced first and second order parameters ($\mu_1 \approx 3.7$ MPa, $\alpha_1 = 0.1$ and $\mu_2 \approx 0.017$ MPa, $\alpha_2 \approx 4.4$). Similarly, A30 required an OG2 in xy and xz directions, in the first direction with $\mu_1 \approx 0.3$ MPa, $\alpha_1 \approx 2$ and $\mu_2 \approx 0.003$ MPa, $\alpha_2 \approx 8$, consistent with strong large-strain nonlinearity. The Y3 model was identified as the most suitable to describe the S40A material in the two directions, as well as TS35Axy and the other directions of MJ materials not captured by OG2. The polynomial Hencky models and Neo-Hookean did not result minimizing the errors when describing any material.

3.4. Properties correlations

Strong correlations were observed between hardness measurements and needle puncturing forces (Fig. 7A-C). In particular, between hardness Shore A and AO measured at 1 s and F_{fri} ($r = 0.946$, $p < 0.001$; $r = 0.933$, $p < 0.001$, respectively) and F_{cut} ($r = 0.784$, $p = 0.012$; $r = 0.817$, $p = 0.004$, respectively), suggesting that the two measures quantify a similar metric.

Important correlations between measured hardness and mechanical properties were identified. At low strains, E_0 correlates moderately with Shore AO ($r = 0.623$, $p = 0.023$), and more with Shore A ($r = 0.858$, $p < 0.001$); similarly, E_{20} correlates with Shore A and Shore AO ($r = 0.885$, $p < 0.001$; $r = 0.642$, $p = 0.018$, respectively), as well as σ_{20} ($r = 0.892$, $p < 0.001$; $r = 0.633$, $p = 0.02$, respectively), confirming that indentation hardness is a reasonable proxy for initial modulus and small deformations. The correlation between E_{100} and σ_{100} resulted weaker with both Shore A ($r = 0.730$, $p = 0.011$; $r = 0.807$, $p = 0.003$, respectively) and AO. Strong correlations were observed between E_0 and friction and cutting forces ($r = 0.938$, $p < 0.001$; $r = 0.901$, $p < 0.001$, respectively), as well as with mechanical parameters at 20% and at 100% elongation ($\sigma_{20} - F_{fri}$: $r = 0.933$, $p < 0.001$; $\sigma_{20} - F_{cut}$: $r = 0.906$, $p < 0.001$). No relevant correlation was observed with mechanical properties at higher strains.

3.5. Biological comparison

3.5.1. Low-strain regime

Multiple synthetic materials fell entirely within the biological reference intervals (Fig. 8, left). The materials EF00, AM01, PG00, DS10M, DS10VF, DS10F, DS10VF and TP emerged as the most potentially suitable to simulate the mechanical behaviour of physiological aorta in circumferential and axial direction, while TS20, A30, KS35, SS936, DS30 being adapt only for the axial direction. For the coronaries, S184, TS35, TS50, S40A and E50Axy resulted good candidates for simulating the physiological conditions, while TS60A was the only good candidate for atherosclerotic conditions. Most of the materials (AM01, PG00, DS10M, DS10F, TP, TS20A, A30, KS35, SS936, DS30, TS35, TS50, S184, S40, E50) resulted potentially suitable to simulate intracranial aneurysms, while a subset of those well replicated cerebral arteries as well (DS10F, TP, TS20A, A30, KS35, TP, SS936, DS30).

3.5.2. High-strain regime

Multi-dimensional material evaluation allowed to identify materials more appropriate to simulate biological tissues at high strains. In this regime, materials presented higher variability. For physiological aorta in the axial direction, E50A resulted as good candidate material ($\bar{d} = 0.50$), followed by TP (1.02), and A30 (1.22). E50A was identified as the closes candidate also in the circumferential direction ($\bar{d} = 0.35$), followed by TP (0.84), S40A (0.89), A30 (0.89); similarly for aortic aneurysms: E50A ($\bar{d} = 0.55$), together with TP (1.09), A30 (1.28), and S40A in zx direction (0.91). For the healthy coronaries, AM01 represented the closest match ($\bar{d} = 0.32$), followed by TP (0.66), PG00 (0.99)

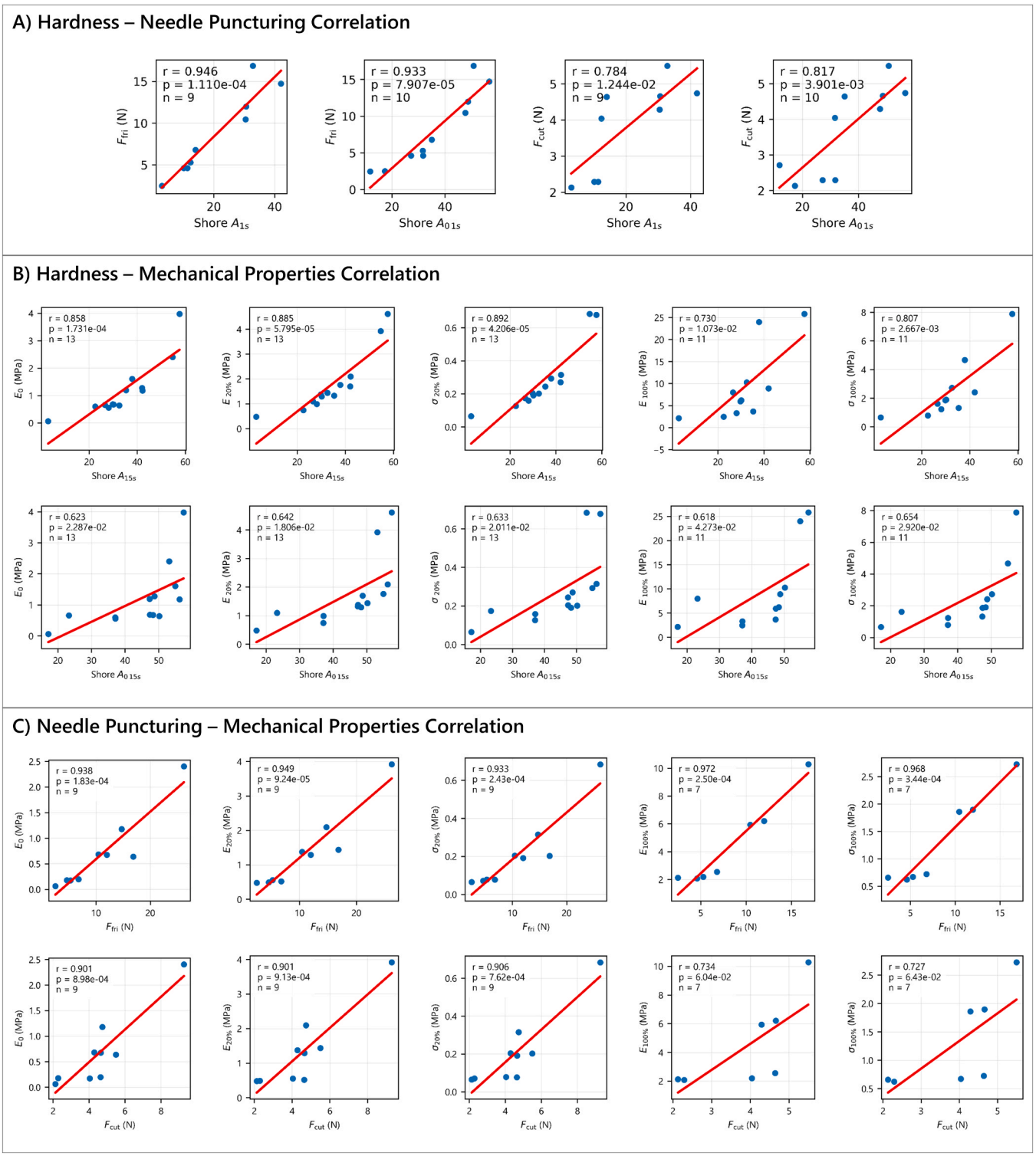


Fig. 7. Correlations between experimental parameters. (A) Correlations between hardness and needle-puncture properties, using one averaged value per material derived from repeated measurements on a single specimen. EF00 could not be measured on the Shore A scale, reducing the corresponding sample size by one. (B) Correlations between hardness and uniaxial tensile properties, with tensile values averaged across specimens and printing orientations for each material. Two materials did not reach 100% strain, reducing the sample size from n = 13 to n = 11 for correlations involving higher-strain properties. (C) Correlations between needle-puncture and uniaxial tensile properties, with an initial sample size of n = 9; for the final two correlations, n was reduced to 7 because two materials did not reach the required strain level.

and E50A (1.60). The latter resulted suitable for the atherosclerotic case as well (0.15), followed by EF00 (0.81), A30 (0.87), and TP (0.92). A wider selection of materials well represented cerebral arteries, from E50A ($\overline{d} = 0.15$), S40A (0.49), TP (0.55), to S184 (0.6), A30 (0.67), and TS60A in zx direction (0.84). These resulted adapt to simulate intracranial aneurysms as well: E50A (0.07); S40A (0.70); TP (0.50); EF00 (0.98).

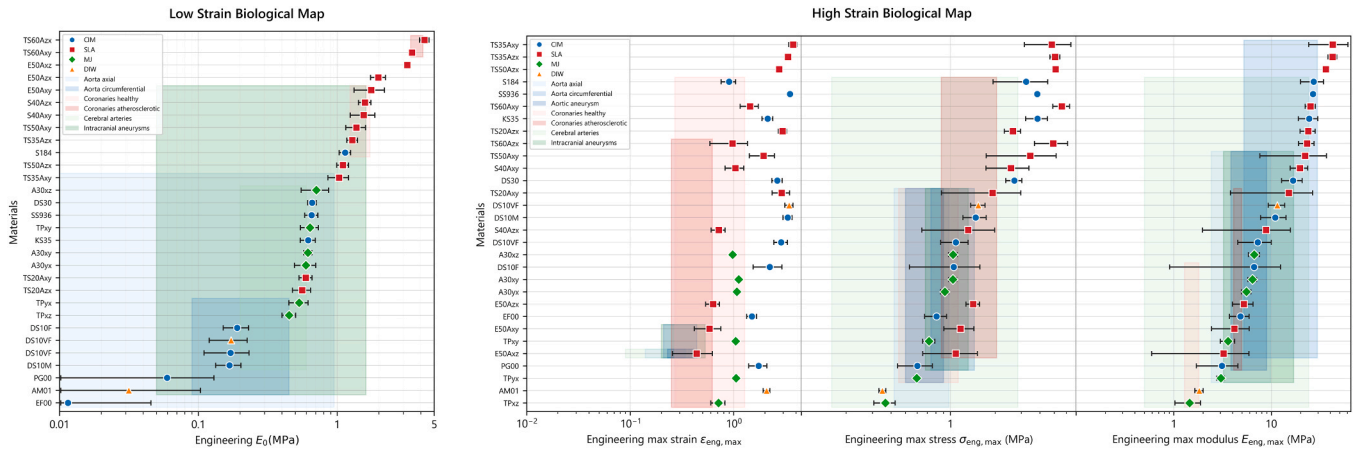


Fig. 8. Decision maps for low and high strain regimes on logarithmic scale. The low strain regime presents the engineering Young modulus as input, and material selection as output. The high strain regime presents the ultimate modulus, ultimate stress and ultimate strain as inputs, and material selection as output. On every map, the ranges of biological parameters are highlighted as shaded areas.

4. Discussion

This study aimed to characterize a total of 30 materials using a combination of three experimental approaches: hardness testing, needle puncture testing, and uniaxial tensile testing, to evaluate hardness, puncture and cutting forces, mechanical parameters, manufacturing methods, and anisotropy. The overall experimental variability was low across all tests, allowing to obtain solid conclusions on the mechanical behaviour of the investigated materials. The results provide a systematic and directly comparable characterization of a broad set of VMM candidates, reducing the influence of laboratory-specific testing differences and enabling relationships among hardness, puncture response, and tensile properties to be identified. The study further provides phenomenological constitutive descriptions suitable for comparative mechanical interpretation and FEM implementation, quantifies anisotropy and similarities across manufacturing technologies, and identifies cases in which different materials or production methods may provide comparable mechanical behaviour. These findings were integrated into a material-selection map linking mechanical properties with literature-derived biological reference ranges. Importantly, the tensile characterization of the synthetic materials was performed on planar specimens and was compared predominantly with biological planar vascular tissue specimens, supporting the validity of the material-level comparison while acknowledging that intact tubular behaviour requires separate application-specific validation. Overall, the study extends the available knowledge from partially characterized individual materials to a comprehensive comparative framework for VMM selection and further validation.

Regarding hardness measurements, most material variants did exhibit Shore A or Shore AO values in proximity to manufacturers' declarations. Measurements performed on rounded square samples and on stacks of three dogbone specimens were found to be interchangeable for most materials on Shore A scale, but not on Shore AO, probably due to higher sensitivity of the second scale to softer materials and smaller hardness variations. While low measurements variability suggests major manufacturing consistency, discrepancies from manufacturers' declared values can be attributed to minor manufacturing variabilities like samples thickness and post-processing settings. Similar deviations were observed in the CIM samples as well, despite their uniform thickness and no post-processing. This suggests that the observed discrepancies might reflect real differences between the tested materials and the manufacturers' reference values. Additionally, the limited differences observed between readings taken after 1 s and 15 s indicate that hardness measurements could be reliably recorded at either time point without significantly affecting the results.

Needle puncture experiments produced a consistent and highly repeatable dataset. The total puncturing and cutting forces were significantly higher than the biological reference, because of several factors: friction forces increase with the length of needle puncturing, as a larger portion of the needle surface interacts with the material; the absence of lubrication likely increased frictional resistance, as the materials behaved in "dry" condition; the measured cutting force represents the force required for the needle to penetrate the full thickness of the material rather than only the surface layer. Apart from the material E50A, the force at a depth of 0.5 mm resulted lower than the biological reference value for all the materials, which was matched instead at a depth of 2.41 mm, suggesting that realistic walled VMM phantoms for puncturing can be produce with that thickness. This finding is relevant for applications where reproducing the native vessel-wall thickness is not necessarily the primary objective, e.g. cannulation or puncture-training phantoms. These can be produced with thickness selected to reproduce a target puncture-force response, and therefore mechanically realistic needle interactions.

Results from uniaxial tensile tests spanned over a broad range of moduli at different strains, while exhibiting hyperelastic behavior overall, with only a few more linear exceptions (E50A, A30 and TP). This allowed to comprehensively characterize the true stress–strain curves of the materials, that resulted higher than engineering values because based on instantaneous cross section, and therefore more informative and appropriate to calculate energy storage and model fitting. The curves also represented strong hyperelastic behaviour at low to moderate strains, already from an extension of 1.2 times the initial length, limiting the extensibility of some materials, that did not double their initial length before failure.

Anisotropy levels resulted comparable between SLA and MJ materials ranging from 0 to about 0.3, except for TS35A that peaked at about 0.55. This is because, differently from FDM, both methods present the same light-driven layer curing, effectively creating a full chemical bond between the last layer and the current one, and obtaining a cohesively built material. These results demonstrate how the use of an isotropic model to fit different printing directions would be inappropriate in most of the included materials, an anisotropic model would be a better choice. For the purposes of the present study, however, anisotropic constitutive models were not fitted because the available data were obtained from independent uniaxial tests along separate directions and were therefore insufficient to reliably identify the coupled parameters required for an anisotropic formulation.

Despite their anisotropy, several materials demonstrated comparable mechanical behavior across manufacturing processes: TP and A30 presented strong similarity, likely attributable to their manufacturing

processes and comparable chemical formulations; DS10VF could be processed using both CIM and DIW with similar mechanical results. These results highlight the potential design flexibility offered by DIW and SLA, albeit within the constraints inherent to that manufacturing technology.

Constitutive modeling provided accurate phenomenological descriptions of the mechanical behavior for all material variants, with low RMSE values across all fits. These fits should not, however, be interpreted as uniquely identified or predictive constitutive models, particularly for materials exhibiting pronounced anisotropy. While the isotropy hypothesis might be appropriate for CIM materials, it does not hold true for SLA, MJ, and DIW materials, as shown above. Indeed, SLA and MJ materials are often best described by different constitutive models depending on the printing direction. However, when considering not only the single best-fitting model but also models with comparable RMSE values, it becomes apparent that additive manufacturing materials can often be described using the same constitutive model family, but with different parameter values, and differences in RMSE only in the second or third significant digit. All materials were well described by constitutive models characterized by the presence of non-negligible higher-order parameters, describing strong hyperelastic behaviours. These phenomenological observations may also support hypotheses regarding the underlying material behaviour. Unlike biological vessels, these materials do not present fiber-reinforced structures, but demonstrate hyperelastic behavior that may be associated to related to conformational entropic elasticity: at low strain levels, polymer chains extend elastically after configurational rearrangement, producing a restoring stress; at higher strains fewer rearrangements happen, and the stress is mainly driven by chain extension, leading to stiffening. In materials with higher polymerization such as E50A, fewer configurational rearrangements might be available, resulting in a quasi-linear stress–-strain response and a stiffening ratio close to unity. Overall, these phenomenological models can be used to formulate testable hypotheses on the microscopic structure of the materials, and the effect on the macroscopic mechanical response. Such hypotheses should be evaluated through further experiments, with more extensive multiaxial and direction-dependent testing particularly necessary for materials exhibiting pronounced anisotropy.

Finally, correlations between the results of the three experimental methods were analyzed to determine whether certain mechanical properties could be inferred indirectly. Strong correlations were observed, highlighting the similarities between tests and their possible interchangeability. The correlation between hardness and puncturing forces can be interpreted after the similar underlying mechanisms, with the hardness results expected to align better with the initial cutting force, that upon increase in applied force results in surface penetration and channelling. The even stronger correlation observed with E_0, E_{20} and σ_{20} supports this thesis, highlighting that the deformation field of the material at indentation involves strains and stresses in a small, yet not negligible range. Similarly, the mechanical values at the beginning, and at 20% of elongation resulted good proxies of friction and cutting forces for the same reasons. These correlations could prove useful to estimate a guessed elastic modulus from the measured hardness on scales Shore A or AO, allowing to use smaller samples and increase the cost-effectiveness of experiments.

Biological vascular tissues are commonly characterized using excised planar specimens under uniaxial loading, as in several of the reference studies considered here. Testing intact cylindrical vessels addresses a different structural response and requires different experimental protocols and, where applicable, dedicated standards (e.g. ISO 7198:206). Therefore, comparisons with biological reference values should primarily be interpreted at the material-property level rather than as direct equivalence to the behaviour of intact vessels. At lower strains, all the manufacturing methods presented suitable materials to replicate biological values, while at higher strains the selection reduces drastically and includes mainly E50A, TP, A30, S40A, and occasionally other formulations. This behaviour emerges as a consequence of the manufacturing methods, being all based on material curing during deposition (CIM, DIW) and between layers (SLA, MJ). As a consequence of the complete material crosslink, failure strains and stresses result really high with respect to human vascular structures, which instead present a layered configuration and response mainly collagen-driven at higher strains. MJ materials, being more fragile by nature, align better to the biological ranges, and are therefore more realistic. Moreover, materials realism at high strains is affected also by the tighter criteria represented by three mechanical parameters evaluated at the same time, instead of one for lower strains. Finally, the need for materials that well replicate high strains behavior was not fully met in this study. Achieving realistic VMM at failure is indeed a higher challenge than at low strains, and the adoption of a manufacturing technology able to replicate the layered nature of vascular structures might succeed better. Nevertheless, a sufficient selection of materials resulted suitable at low strain regime, providing choice flexibility according to the application.

It should also be noted that different applications might require different sample sizes: thickness, geometry, and constraints can alter the haptic sensation and the interaction with surgical devices, resulting in different mechanics than the standardized measurements done on isolated specimens. In addition, surrounding tissues in vivo may further modify the effective mechanical behavior of the structure. The proposed material map of Fig. 8 represents a first iteration in supporting material choice, and can expanded with additional information. Material choice should ultimately be refined according to the specific geometry and application. In this process, interaction with clinicians is essential, as their feedback on tactile realism and device interaction provides insights that cannot be fully captured through mechanical testing alone.

This study presents few potential limitations. First, the selection of materials was primarily based on availability, previous literature, and preliminary observations. Despite the current investigation being the largest to the best of authors' knowledge, the aim was not to provide an exhaustive review of all possible materials but rather to characterize a representative set of candidates. Some experimental constraints were also present: needle puncture tests could not be performed for all materials due to difficulties in producing suitable samples of the materials not included. In principle, this limitation could be mitigated by manufacturing thin material sheets instead of cylindrical samples; however, this approach is more challenging for additive manufacturing technologies such as SLA, DIW and MJ compared with CIM, because of their layered nature. Additionally, puncture forces measured on the relatively thick specimens used in this study should not be directly extrapolated to anatomically thin vessel walls; future application-specific validation should therefore assess needle–tissue interaction in phantoms with physiologically representative wall thicknesses. From a statistical perspective, the study is limited by the use of a single independently fabricated specimen per material for hardness and needle-puncture testing, with repeated measurements performed within each specimen. Future studies including multiple independent specimens per material would enable more robust estimation of between-specimen variability and support stronger inferential statistical analyses. During uniaxial tensile testing, a small number of specimens slipped out of the clamps and had to be excluded from the analysis, resulting in four valid samples instead of five for certain materials. This did not result in results invalidity, confirmed by strong measurements agreement. Improved clamping systems might reduce this issue in future experiments. More generally, manufacturability represented a significant constraint, as producing specimens with certain orientations proved difficult (e.g. DIW), limiting the range of configurations that could be evaluated and limiting anisotropy assessment of every manufacturing technology (Fig. 2). In addition, even though the anisotropy analysis revealed that anisotropic constitutive models should be used to characterize simultaneously different printing directions, only isotropic models were used in this study, and for one printing direction at a time. To better employ anisotropic models, more complex tensile tests might be appropriate,

like biaxial or multi-axial tensile tests. Finally, the strain rate used in the uniaxial tensile tests was relatively high compared with quasi-static testing conditions, which may have influenced the measured mechanical response. This could result in harder apparent material behavior because of the overlap of elastic and viscous effects, and a failure at lower strains. Despite that, comparison between materials is still valid, and the errors introduced at low strains might be negligible. However, discrepancies observed between experimentally measured hardness values and those reported by manufacturers suggest that manufacturer-provided mechanical data may also require careful verification. Comparison with biological materials should also be interpreted with caution, given the inherent variability of biological tissues and their dependence on factors such as experimental conditions, age, pathological state, loading direction, strain rate, and testing methodology. The biological values reported in this study were therefore used as reference ranges for comparative material screening rather than as absolute target values. Furthermore, unlike standardized flat testing specimens, native vessels exhibit complex geometries that can influence their apparent mechanical and viscoelastic response, introducing an additional source of variability when comparing biological tissues with synthetic materials. This study did not include a complete viscoelastic characterization, as the focus was placed on responses relevant for procedural and training applications where phantoms are mainly intended to reproduce immediate mechanical interaction and haptic feedback. However, viscoelastic behaviours may become relevant in different surgical applications or under prolonged, cyclic, or rate-dependent loading conditions, and future work should investigate these aspects.

Validation in representative vascular geometries represents an important subsequent step in assessing the applicability of candidate materials. Previous work from our group has demonstrated one possible approach to phantom-level validation. [45] However, the required level of anatomical and mechanical realism depends on the intended application. Procedural training, preoperative planning, and device testing may impose different requirements in terms of geometry, wall thickness, deformation, interaction with surrounding structures, and overall mechanical response. Consequently, validation protocols should be defined according to the specific requirements of the intended use, rather than relying on a single universal definition of vascular phantom realism.

5. Conclusion

We investigated the most commonly used VMM for vascular tissues, and characterized them with standardized and systematic hardness, needle puncturing and uniaxial tensile tests. Results showed that materials spanned over a wide range of properties, from soft, energy absorbing hyperelastic variants to hard, quasi-linear variants. Materials from different manufacturing technologies resulted anisotropic, and a selection presented similarities making them interchangeable. Correlations between material properties allowed to reliably infer approximated mechanical parameters from simpler test. Comparison with biological reference values identified suitable candidate materials for applications in neurovascular and cardiovascular medicine, both at low and high strain regimes. By evaluating multiple materials and manufacturing technologies within a common experimental framework, this study addresses the lack of comprehensive and directly comparable mechanical data and provides a basis for defining more objective criteria for material selection in vascular phantom development.

CRediT authorship contribution statement

Lorenzo Civilla: Writing – original draft, Visualization, Validation, Software, Resources, Methodology, Investigation, Funding acquisition, Formal analysis, Data curation, Conceptualization. **Maria Riviello:** Software, Investigation, Formal analysis, Data curation. **Itzany Montiel-Saletović:** Investigation, Formal analysis, Data curation. **Ewald Unger:** Resources, Methodology, Conceptualization. **Markus Königshofer:** Resources, Methodology. **Akin Gursoy:** Resources. **Luis Mäder:** Resources. **Laszlo Jaksa:** Resources, Methodology. **Andrea Lorenz:** Writing – review & editing, Resources. **Erik Kornfellner:** Writing – review & editing, Methodology. **Diego Gallo:** Writing – review & editing, Supervision. **Francesco Moscato:** Writing – review & editing, Validation, Supervision, Resources, Project administration, Methodology, Funding acquisition, Conceptualization.

Declaration of Generative AI and AI-assisted technologies in the writing process

Generative Artificial Intelligence (AI) tools were used during the execution of this study and the writing of this article: ChatGPT 5.5 (OpenAI, San Francisco, CA, USA) was employed to support sentence reformulation of small parts of the text, then independently revised and corrected by the authors; Codex CLI (based on GPT-5.5, OpenAI) was used to support the production of python scripts for data analysis, and python scripts run to produce Figs. 6 and 8, then independently reviewed, validated and executed offline on a local machine to ensure data privacy. The generative AI tools mentioned above were used under configurations ensuring privacy and excluding data use for further model training.

Sources of funding

This work was supported by the Austrian Research Promotion Agency (FFG) under the project “Additive Manufacturing for M3dical RESearch, M3dRES”, nr. 858060; Austria Wirtschaftsservice GmbH (AWS) under the project “New Patient-Specific Surgical Simulator”, nr. P2410019.

Disclosure statement / declaration of interest statement

At the moment of study execution, Akin Gursoy and Luis Mäder were employed at Spectroplast AG, and Laszlo Jaksa and Andrea Lorenz were employed at ACMIT GmbH, and bot supplied part of the material samples investigated. Data analysis, interpretation and report were performed independently and uninfluenced by commercial interests.

Declaration of Competing Interest

The authors declare the following financial interests/personal relationships which may be considered as potential competing interests: Francesco Moscato reports financial support was provided by Austrian Research Promotion Agency. Lorenzo Civilla reports financial support was provided by Austria Business Service. Francesco Moscato, Lorenzo Civilla, Ewald Unger and Markus Königshofer are listed inventors on the patent application #EP4721040A1 owned by the Medical University of Vienna.

Acknowledgments

No acknowledgments apply to this manuscript.

Appendix A. Supporting information

Supplementary data associated with this article can be found in the online version at doi:10.1016/j.mtcomm.2026.116579.

Data Availability

Link to the data provided in the manuscript: https://doi.org/10.6084/m9.figshare.32779662

References

[1] J. Burke, The future of surgery: technology enhanced surgical training report, Bull. R. Coll. Surg. Engl. 103 (2021) 014–017, https://doi.org/10.1308/rcsbull.TB2021.6.

[2] N. Seam, A.J. Lee, M. Vennero, L. Emlet, Simulation training in the ICU, Chest 156 (6) (2019) 1223–1233, https://doi.org/10.1016/j.chest.2019.07.011.

[3] Q. Zeng, K. Wang, W. xin Liu, et al., Efficacy of high-fidelity simulation in advanced life support training: a systematic review and meta-analysis of randomized controlled trials, BMC Med. Educ. 23 (1) (2023) 664, https://doi.org/10.1186/s12909-023-04654-x.

[4] H. Nisar, J. Moore, R. Piazza, E. Maneas, E.C.S. Chen, T.M. Peters, A simple, realistic walled phantom for intravascular and intracardiac applications, Int. J. CARS 15 (9) (2020) 1513–1523, https://doi.org/10.1007/s11548-020-02201-3.

[5] R. Jafary, S. Armstrong, T. Byrne, A. Stephens, V. Pellegrino, S.D. Gregory, Fabrication and Characterization of Tissue-Mimicking Phantoms for Ultrasound-Guided Cannulation Training, ASAIO J. 68 (7) (2022) 940–948, https://doi.org/10.1097/MAT.0000000000001593.

[6] K. Dakok, M. Matjafri, N. Suardi, A. Oglat, S. Nabasu, A review of carotid artery phantoms for doppler ultrasound applications, J. Med. Ultrasound 29 (3) (2021) 157, https://doi.org/10.4103/JMU.JMU_164_20.

[7] Dodier P. An evaluation of physical and augmented patient-specific intracranial aneurysm simulators on microsurgical clipping performance and skills: a randomized controlled study. *Neurosurg Focus*. 56(1):E9. doi:10.3171/2023.10.FOCUS23640.

[8] J. Coles-Black, D. Bolton, D. Robinson, J. Chuen, Utility of 3D printed abdominal aortic aneurysm phantoms: a systematic review, ANZ J. Surg. 91 (9) (2021) 1673–1681, https://doi.org/10.1111/ans.16763.

[9] F.A. Rocha, L.M. Ribas, P.I. Sassaki-Neto, N. De-Luccia, Experimental comparative study of arterial implants made of silicone reinforced with polyester fabric and expanded polytetrafluoroethylene (PTFE) in rabbits aorta, Rev. Col. Bras. Cir. 48 (2021) e20202587, https://doi.org/10.1590/0100-6991e-20202587.

[10] A. Larena-Avellaneda, G. Dittmann, C. Haacke, et al., Silicone-Based Vascular Prosthesis: Assessment of the Mechanical Properties, Ann. Vasc. Surg. 22 (1) (2008) 106–114, https://doi.org/10.1016/j.avsg.2007.09.003.

[11] D. Chen, S. Liang, Z. Li, et al., A Mock Circulation Loop for In Vitro Hemodynamic Evaluation of Aorta: Application in Aortic Dissection, J. Endovasc. Ther. 29 (1) (2022) 132–142, https://doi.org/10.1177/15266028211034863.

[12] C.K. Ho, A.J.Y. Chee, B.Y.S. Yiu, A.C.O. Tsang, K.W. Chow, A.C.H. Yu, Wall-Less Flow Phantoms With Tortuous Vascular Geometries: Design Principles and a Patient-Specific Model Fabrication Example, IEEE Trans. Ultrason. Ferroelectr. Freq. Control. 64 (1) (2017) 25–38, https://doi.org/10.1109/TUFFC.2016.2636129.

[13] D.B. Camasão, D. Mantovani, The mechanical characterization of blood vessels and their substitutes in the continuous quest for physiological-relevant performances. A critical review, Mater. Today Bio 10 (2021) 100106, https://doi.org/10.1016/j.mtbio.2021.100106.

[14] M. Błaszczyk, R. Jabbar, B. Szmyd, M. Radek, 3D Printing of Rapid, Low-Cost and Patient-Specific Models of Brain Vasculature for Use in Preoperative Planning in Clipping of Intracranial Aneurysms, J. Clin. Med. 10 (6) (2021) 1201, https://doi.org/10.3390/jcm10061201.

[15] S. Zhao, W. Wu, S. Samant, et al., Patient-specific computational simulation of coronary artery bifurcation stenting, Sci. Rep. 11 (1) (2021) 16486, https://doi.org/10.1038/s41598-021-95026-2.

[16] A. Pionteck, B. Pierrat, S. Gorges, J.N. Albertini, S. Avril, Evaluation and verification of fast computational simulations of stent-graft deployment in endovascular aneurysmal repair, Front. Med. Technol. 3 (2021) 704806, https://doi.org/10.3389/fmedt.2021.704806.

[17] D.P.G. Nilsson, M. Holmgren, P. Holmlund, et al., Patient-specific brain arteries molded as a flexible phantom model using 3D printed water-soluble resin, Sci. Rep. 12 (1) (2022) 10172, https://doi.org/10.1038/s41598-022-14279-7.

[18] Q.Z. Chi, L.Z. Mu, Y. He, Y. Luan, Y.C. Jing, A Brush–Spin–Coating Method for Fabricating In Vitro Patient-Specific Vascular Models by Coupling 3D-Printing, Cardiovasc. Eng. Tech. 12 (2) (2021) 200–214, https://doi.org/10.1007/s13239-020-00504-9.

[19] N. Emiliani, R. Porcaro, G. Pisaneschi, et al., Post-printing processing and aging effects on Polyjet materials intended for the fabrication of advanced surgical simulators, J. Mech. Behav. Biomed. Mater. 156 (2024) 106598, https://doi.org/10.1016/j.jmbbm.2024.106598.

[20] A.H. Bharucha, J. Moore, P. Carnahan, et al., Three-dimensional printing in modelling mitral valve interventions, Echo Res. Pract. 10 (1) (2023) 12, https://doi.org/10.1186/s44156-023-00024-x.

[21] S. Duraivel, D. Laurent, D.A. Rajon, et al., A silicone-based support material eliminates interfacial instabilities in 3D silicone printing, Science 379 (6638) (2023) 1248–1252, https://doi.org/10.1126/science.ade4441.

[22] M. Gort, E. Morlec, D. Gwerder, P. Schuetz, M. Camenzind, M. Meboldt, O_2 permeability of additively manufactured silicone membranes, J. Appl. Polym. Sci. 140 (30) (2023) e54079, https://doi.org/10.1002/app.54079.

[23] M.M. Duran, G. Moro, Y. Zhang, A. Islam, 3D printing of silicone and polyurethane elastomers for medical device application: A review, Adv. Ind. Manuf. Eng. 7 (2023) 100125, https://doi.org/10.1016/j.aime.2023.100125.

[24] O. Grimaldo Ruiz, M. Rodriguez Reinoso, E. Ingrassia, et al., Design and Mechanical Characterization Using Digital Image Correlation of Soft Tissue-Mimicking Polymers, Polymers 14 (13) (2022) 2639, https://doi.org/10.3390/polym14132639.

[25] S. Lin, G. Tarris, C. Bernard, et al., Biomechanical properties of 3D printable material usable for synthetic personalized healthy human aorta, ijb 9 (4) (2023) 736, https://doi.org/10.18063/ijb.736.

[26] Y. Liu, Q. Gao, S. Du, et al., Fabrication of cerebral aneurysm simulator with a desktop 3D printer, Sci. Rep. 7 (1) (2017) 44301, https://doi.org/10.1038/srep44301.

[27] E. Lanzarone, S. Marconi, M. Conti, et al., Hospital factory for manufacturing customised, patient-specific 3D anatomo-functional models and prostheses, in: T. Tolio, G. Copani, W. Terkaj (Eds.), Factories of the Future. Springer International Publishing, 2019, pp. 233–254, https://doi.org/10.1007/978-3-319-94358-9_11.

[28] I.D. Johnston, D.K. McCluskey, C.K.L. Tan, M.C. Tracey, Mechanical characterization of bulk Sylgard 184 for microfluidics and microengineering, J. Micromech. Microeng. 24 (3) (2014) 035017, https://doi.org/10.1088/0960-1317/24/3/035017.

[29] P. Aigner, E. Sella Bart, S. Panfili, et al., Quantification of paravalvular leaks associated with TAVI implants using 4D MRI in an aortic root phantom made possible by the use of 3D printing, Front. Cardiovasc. Med. 10 (2023) 1083300, https://doi.org/10.3389/fcvm.2023.1083300.

[30] M. Zare, E.R. Ghomi, P.D. Venkatraman, S. Ramakrishna, Silicone-based biomaterials for biomedical applications: Antimicrobial strategies and 3D printing technologies, J. Appl. Polym. Sci. 138 (38) (2021) 50969, https://doi.org/10.1002/app.50969.

[31] Ionita C.N., Mokin M., Varble N., et al. Challenges and limitations of patient-specific vascular phantom fabrication using 3D Polyjet printing. In: Molthen R.C., Weaver J.B., eds. 2014:90380M. doi:10.1117/12.2042266.

[32] L. Jaksa, D. Pahr, G. Kronreif, A. Lorenz, Calibration Dependencies and Accuracy Assessment of a Silicone Rubber 3D Printer, Inventions 7 (2) (2022) 35, https://doi.org/10.3390/inventions7020035.

[33] L. Jaksa, D. Pahr, G. Kronreif, A. Lorenz, Development of a Multi-Material 3D Printer for Functional Anatomic Models, IJB 7 (4) (2024) 420, https://doi.org/10.18063/ijb.v7i4.420.

[34] R.S. Rivlin, Taylor GI. Large elastic deformations of isotropic materials. I. Fundamental concepts, Philos. Trans. R. Soc. Lond. Ser. A Math. Phys. Sci. 240 (822) (1997) 459–490, https://doi.org/10.1098/rsta.1948.0002.

[35] A. Bower. Applied Mechanics of Solids. Applied Mechanics of Solids. 2025. Accessed June 23, 2026. https://solidmechanics.org/index.html.

[36] J.P. Vande Geest, M.S. Sacks, D.A. Vorp, The effects of aneurysm on the biaxial mechanical behavior of human abdominal aorta, J. Biomech. 39 (7) (2006) 1324–1334, https://doi.org/10.1016/j.jbiomech.2005.03.003.

[37] Z. Li, M. Pei, J. Zhang, N. Liu, J. Wang, D. Zou, A study to characterize the mechanical properties and material constitution of adult descending thoracic aorta based on uniaxial tensile test and digital image correlation, Front. Bioeng. Biotechnol. 11 (2023) 1178199, https://doi.org/10.3389/fbioe.2023.1178199.

[38] J. Xiong, S.M. Wang, W. Zhou, J.G. Wu, Measurement and analysis of ultimate mechanical properties, stress-strain curve fit, and elastic modulus formula of human abdominal aortic aneurysm and nonaneurysmal abdominal aorta, J. Vasc. Surg. 48 (1) (2008) 189–195, https://doi.org/10.1016/j.jvs.2007.12.053.

[39] H. Chen, G.S. Kassab, Microstructure-based biomechanics of coronary arteries in health and disease, J. Biomech. 49 (12) (2016) 2548–2559, https://doi.org/10.1016/j.jbiomech.2016.03.023.

[40] A.P. Ebrahimi, Mechanical Properties of Normal and Diseased Cerebrovascular System, J. Vasc. Interv. Neurol. 2 (2) (2009) 155–162.

[41] K. Truchel, K. Wojtas, R. Rzepliński, et al., Statistical analysis of the measured strength parameters of the fresh main intracranial arteries, Front. Bioeng. Biotechnol. 13 (2025) 1554674, https://doi.org/10.3389/fbioe.2025.1554674.

[42] J.R. Cebral, X. Duan, B.J. Chung, C. Putman, K. Aziz, A.M. Robertson, Wall Mechanical Properties and Hemodynamics of Unruptured Intracranial Aneurysms, AJNR Am. J. Neuroradiol. 36 (9) (2015) 1695–1703, https://doi.org/10.3174/ajnr.A4358.

[43] I. Elgezua, S. Song, Y. Kobayashi, M. Fujie, Event. Classif. Percutaneous Treat. Based Needle Insert Force Pattern Anal. (2013) 293, https://doi.org/10.1109/ICCAS.2013.6703910.

[44] D.W. Laurence, H. Homburg, F. Yan, et al., A pilot study on biaxial mechanical, collagen microstructural, and morphological characterizations of a resected human intracranial aneurysm tissue, Sci. Rep. 11 (1) (2021) 3525, https://doi.org/10.1038/s41598-021-82991-x.

[45] L. Civilla, P. Dodier, M.C. Palumbo, et al., Development and assessment of case-specific physical and augmented reality simulators for intracranial aneurysm clipping, 3D Print. Med. 10 (1) (2024) 30, https://doi.org/10.1186/s41205-024-00235-w.